PAPER • OPEN ACCESS

Investigation of the *B*-field-induced widening of the donor-electron energy distribution in n-doped (Zn,Mn)Se by resonant electron spin-flip Raman spectroscopy

View the article online for updates and enhancements.

Journal of Physics Communications

CrossMark

Investigation of the *B*-field-induced widening of the donor-electron energy distribution in n-doped (Zn,Mn)Se by resonant electron spin-flip Raman spectroscopy

A G Knapp[1], M Hetterich[2] and J Geurts[1]

[1] Physikalisches Institut (EP3), University of Würzburg, D-97074 Würzburg, Germany
[2] Institute of Applied Physics and DFG Center for Functional Nanostructures (CFN), Karlsruhe Institute of Technology (KIT), D-76131 Karlsruhe, Germany

E-mail: aknapp@physik.uni-wuerzburg.de

Abstract

In n-doped diluted magnetic semiconductors the (s-d)-exchange-induced shift of the donor electron levels in an external *B*-field is expected to be subject to local fluctuations due to the statistical distribution of the magnetic ions. We investigated this phenomenon by resonant electron spin-flip Raman spectroscopy (ESFRS) on (Zn,Mn)Se:Cl samples with Mn contents up to 0.07 and n-dopant concentrations up to $1.3 \times 10^{18} \, cm^{-3}$. The profile of the ESFRS efficiency versus photon energy shows a pronounced resonance, comprising two contributions due to the donor-bound exciton (D^0,X) and the free-exciton (X^0) as the intermediate states for the ESFRS process. The exchange-induced widening of the electron energy distribution is clearly reflected in the spectral width of the (D^0,X) resonance contribution. A distinct *B*-field-induced broadening occurs, typically by a factor of two between $B \sim 1 \, T$ and $B = 7 \, T$. By employing the statistics of the local Mn concentration fluctuations, the radius of the donor-bound exciton (D^0,X) is evaluated from this broadening, yielding (D^0,X) radii from 1.75 nm to 5.90 nm and showing a decrease with increasing Mn content as well as dopant concentration.

1. Introduction

Paramagnetic doped diluted magnetic semiconductors (DMS) based on II-VI compounds, such as e.g. n-doped $Zn_{1-x}Mn_xSe$ ($x < 0.1$), are of high relevance for fundamental studies of the magnetic impact on electronic transport and optical properties, because they facilitate the independent variation of the magnetic Mn^{2+}-ion concentration and the dopant ion content (e.g. Cl^-) [1].

When an external *B*-field is applied to such a paramagnetic DMS material, an extraordinarily large spin splitting in the conduction- and valence band levels is induced, which is boosted by the Mn d-levels through (s-d)- and (p-d)-exchange interaction with exchange energy constants above 0.2 eV [1, 2]. In terms of g-factors, this implies values beyond 100 [3]. As for electronic transport, a very pronounced magnetoresistance occurs [4], which is especially relevant in the doping range slightly below the Mott-transition density, where transport is dominated by hopping processes in the impurity band [5–7]. Moreover, the huge spin splitting leads to a highly intriguing behavior in optical properties. Among the most prominent optical features are a giant Faraday rotation in transmission [8, 9] and giant Zeeman splittings beyond 100 meV of exciton transition peaks in photoluminescence spectra [10].

For the direct observation of the *B*-field-induced splitting of energy levels with different spin orientations, magneto-Raman spectroscopy of spin-flip transitions has become a well-established technique. Not only the Mn^{2+} paramagnetic resonance, i.e., $\Delta m_S = +1$ transitions from the $^6S_{5/2}$ ground-state of the localized Mn^{2+} $3d^5$-orbitals was analyzed [11], but also electronic spin-flip Raman scattering (ESFRS), probing spin-flip transitions of donor-bound or free electrons [12–14]. Thus, ESFRS provides an immediate access to the *B*-

Table 1. Parameters of the $Zn_{1-x}Mn_xSe$:Cl samples in this study: Mn content x, dopant concentration N_{Cl}, and ZnSe layer thickness.

sample	Mn x	N_{Cl} (cm^{-3})	thickness (μm)
A	0.07	$<10^{16}$	0.70
B	0.05	2.0×10^{17}	0.93
C	0.05	4.2×10^{17}	1.04
D	0.05	1.3×10^{18}	0.90
E	0.01	4.3×10^{17}	1.05

induced electron spin splitting energy value, e.g. for the direct determination of the (s-d)-exchange energy value [15–17].
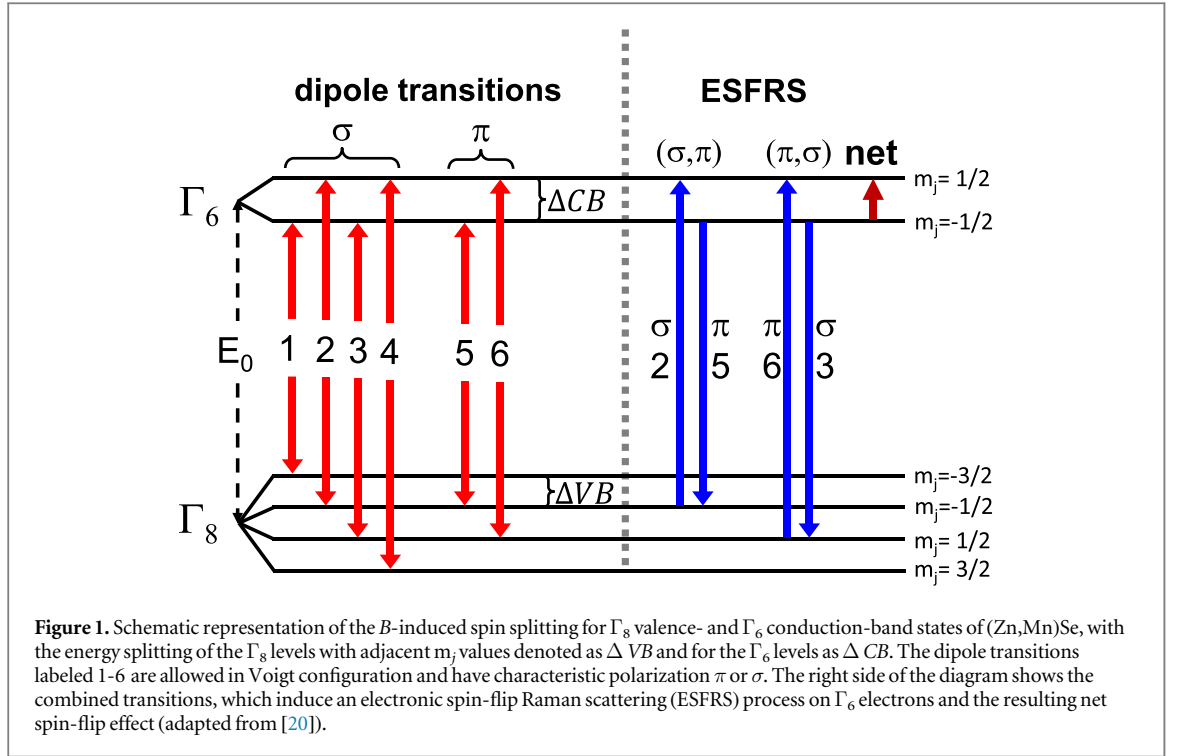
Generally, a substantial enhancement of the efficiency of Raman scattering processes can be achieved by tuning the exciting laser wavelength into resonance with an electronic interband transition: Resonant Raman Spectroscopy (RRS) [18, 19]. This resonant enhancement applies especially for ESFRS, which is a two-step process, and therefore has a double-resonant character [3, 20]. The very pronounced resonance-induced enhancement of the ESFRS-efficiency yields two important advantages: (i) a very high material-selective detection sensitivity, and (ii) the spectral width of the scattering-efficiency resonance profile gives access to the energy-distribution width of the electronic states which are involved in the Raman scattering process.

Therefore, we have exploited the resonance behavior of ESFRS to study the Cl-doped DMS (Zn,Mn)Se with doping concentrations up to $1.3 \times 10^{18}\,cm^{-3}$, to get further insight into the energy distribution of the donor electron states and the corresponding donor-bound excitons (D^0,X), and moreover, the influence of the external B-field on this distribution. Hence the main focus of this paper is on the development of the width of the ESFRS resonance profile for external magnetic fields from 1 T to 7 T. We observe a distinct broadening, which is explained in terms of a widening of the energy distribution of the Cl-dopant electron levels due to the statistical fluctuations of the local Mn content in their immediate vicinity. Our results corroborate the theoretical model description of the giant-magneto resistance of DMS by a broadening of the energy distribution of the donor states due to the statistical distribution of the Mn atoms [4, 7]. Moreover, from the quantitative evaluation of the B-induced profile broadening the radii of the bound exciton states (D^0,X) are determined.

2. Experimental

The samples in this study were epitaxial layers of n-type $Zn_{1-x}Mn_xSe$ with x = 0.01, x = 0.05 and x = 0.07, grown by molecular beam epitaxy (MBE) on semi-insulating (100) GaAs substrates, using chlorine as n-type dopant, provided by evaporating $ZnCl_2$. The layer structures consist of an undoped ZnSe buffer, followed by the n-type $Zn_{1-x}Mn_xSe$:Cl layer with a thickness of about 1 μm [21]. Mn atoms are isovalently substituted for Zn atoms and the Cl donor atoms occupy Se sites. The doping was between nominally undoped and $N_{Cl} = 1.3 \times 10^{18}\,cm^{-3}$. The Mn content was verified by x-ray diffraction (XRD) analysis. The relevant parameters of the samples are listed in table 1.

As excitation light source for the Raman spectroscopy, a UV-pumped dye laser was employed, operated with stilbene 3, covering the spectral range of incident photon energies E_{in} from 2.77 eV to 2.85 eV. This enabled its tuning into resonance with the fundamental bandgap E_0 of $Zn_{1-x}Mn_xSe$ with x $\leqslant$ 0.07 near 2.81 eV [22]. The Raman measurements were performed in backscattering geometry, i.e., the standard geometry which is commonly used for Raman scattering on opaque samples. The spectra were recorded with a Dilor XY triple spectrometer, equipped with a Peltier-cooled CCD detector (ANDOR iDus series). The integration time of each spectrum was typically up to 120 s. The intensity of the spin-flip Raman peak in each individual spectrum was calibrated by employing the main photoluminescence peak as an internal normalization standard. The external magnetic field was varied in a split-coil superconducting magnet between 0 and $B = 7$ Tesla, oriented parallel to the sample surface. This implies that the B-field direction is perpendicular to the propagation directions of the incoming and the scattered light, i.e., in the geometry of the Voigt effect [23]. Therefore it is commonly referred to as the Voigt configuration [1, 2, 24]. The polarization configurations of the incident and the scattered light, denoted as (e_i,e_s) in Porto's notation [25], were (σ,π) and (π,σ), where π and σ represent the directions parallel and perpendicular to the B-field, respectively. The samples were immersed in suprafluid liquid helium at temperature T = 1.6 K.

Figure 1. Schematic representation of the *B*-induced spin splitting for Γ_8 valence- and Γ_6 conduction-band states of (Zn,Mn)Se, with the energy splitting of the Γ_8 levels with adjacent m_j values denoted as ΔVB and for the Γ_6 levels as ΔCB. The dipole transitions labeled 1-6 are allowed in Voigt configuration and have characteristic polarization π or σ. The right side of the diagram shows the combined transitions, which induce an electronic spin-flip Raman scattering (ESFRS) process on Γ_6 electrons and the resulting net spin-flip effect (adapted from [20]).

3. Results and discussion

In an external magnetic field *B*, the giant Zeeman splitting of the energy levels at the valence-band (VB) maximum as well as the conduction band (CB) minimum in DMS due to the (s-d)- and (p-d)-interaction is described in the mean-field approximation by:

$$VB: E(B) = \frac{1}{3}m_j \cdot N_0\beta \cdot x_{eff} \cdot \langle S_z(B) \rangle \tag{1}$$

$$CB: E(B) = E_0 + m_j \cdot N_0\alpha \cdot x_{eff} \cdot \langle S_z(B) \rangle \tag{2}$$

where E_0 is the gap energy in the absence of an external magnetic field, m_j is the magnetic quantum number ($m_j = \pm 1/2$ for CB-states, $m_j = \pm 1/2; \pm 3/2$ for VB-states), x_{eff} is the Mn concentration x, reduced by an x-dependent correction factor due to the antiferromagnetic d-d interaction between nearest-neighbor Mn ions [1], and $N_0\alpha$ and $N_0\beta$ are the exchange constants for the (s-d) and (p-d)-exchange interaction, respectively, with $N_0\alpha = 260$ meV and $N_0\beta = -1310$ meV for $Zn_{1-x}Mn_xSe$ [26].

$\langle S_z(B) \rangle$ represents the mean-field average spin value of the Mn^{2+} ions, which is described by the modified Brillouin function $B_J(B/T)$ for angular momentum J $= 5/2$ [1]:

$$\langle S_z(B) \rangle = -\frac{5}{2}B_{5/2}\left[\frac{5g_{Mn}\mu_B B}{2k_B(T + T_{AF})}\right]. \tag{3}$$

Here, *T* is the sample temperature, for our experiments 1.6 K, $g_{Mn} = 2$ is the g factor of the Mn d states, T_{AF} is a phenomenological *x*-dependent temperature correction parameter for the effective Mn temperature for considering also the antiferromagnetic interaction beyond nearest neighbor Mn ions [1] and can be calculated by $T_{AF}(x) = 47.2x - 281x^2 + 714x^3$ [10], which results in $T_{AF}(x = 0.01) = 0.50$ K and $T_{AF}(x = 0.05) = 1.75$ K. When the Mn ions are randomly positioned on the cation sites, for $x \leqslant 0.1$, x_{eff} can be written as [27]:

$$x_{eff}(x) = \frac{1}{5}x \cdot (x - 1)^{12} \cdot \{5 + 2x^2 \cdot (x - 1)^{10} \cdot [109 + 15x \cdot (5x - 12)]\} \tag{4}$$

For chemical Mn concentrations $x \leqslant 0.01$, the deviation between x and x_{eff} can be neglected, but already for $x = 0.05$, x_{eff} is reduced to 0.03, meaning that only 60% of the Mn^{2+} ions unfold their magnetic impact.

The implications of this *B*-induced level splitting for the optical behavior at the fundamental gap of (Zn,Mn) Se are illustrated in figure 1, which shows the relevant energy levels $|VB, m_j\rangle$ and $|CB, m_j\rangle$ in an external *B*-field, and on the left side the corresponding optical dipole transitions in Voigt configuration. The *B*-dependent energy separations between adjacent m_j-levels of the CB- and VB states are denoted as ΔCB and ΔVB, respectively. It should be noted that in the following the denominations CB- and VB state are also applied for the corresponding exciton states constituents of free or donor-bound excitons, i.e. (X^0) and (D^0,X). Between the Γ_8 VB states and

the Γ_6 CB states, six transitions are allowed with $\Delta m_j = 0$ or ± 1, corresponding to the light polarization direction parallel (π) or perpendicular (σ) to the *B*-field direction, respectively. These transitions give rise to characteristic features in the photoluminescence (PL) spectrum with increasing spectral splitting in the external *B*-field according to equations (1) and (2). The relative intensities of these spectral features are governed by the occupancy of the involved states and the selected polarization of the light. Possible ESFRS processes are shown in the right side of figure 1. As a two-step inelastic light scattering process with a net electron spin transfer $\Delta m_j = 1$, ESFRS can be realized as a combination of the dipole transitions $2\Uparrow$ (from $|VB, -1/2\rangle$ to $|CB, +1/2\rangle$) and $5\Downarrow$ (from $|CB, -1/2\rangle$ to $|VB, -1/2\rangle$) with polarization (σ,π), but also as a combination of $6\Uparrow$ and $3\Downarrow$ with polarization (π,σ). In both cases, in the first step, an electron is excited to the upper CB state and a hole is created in the VB. A dopant electron recombines from the lower CB state with the VB hole by emitting a Stokes-shifted photon. The energy difference between the incident and scattered photon, i.e., the Stokes shift of the ESFRS peak in the Raman spectrum, exactly equals the *B*-induced CB splitting ΔCB. Thus, its *B*-field dependence directly reflects the Brillouin-function behavior according to equation (2).

The dominant term in the corresponding formula of the scattering cross section $\partial \sigma / \partial \omega$, i.e., the probability of the ESFRS scattering process, reads as follows [2]:

$$\left(\frac{\partial \sigma}{\partial \omega}\right)_{ESFRS} \propto \left[\frac{\langle f|p_\beta|e\rangle \langle e|p_\alpha|0\rangle}{E_e - \hbar\omega_i}\right]^2 \tag{5}$$

Here p_α and p_β are the vector components of the dipole operators of the incident and scattered radiation. The states $|0\rangle$, $|e\rangle$, and $|f\rangle$ are the initial, intermediate (excited), and final electronic state, respectively. $\hbar\omega_i$ is the incident photon energy, and E_e is the excitation energy for of the intermediate electronic state.

By tuning the incident photon energy $\hbar\omega_i$, its match with E_e can be achieved, in order to fulfill the resonance condition for the excitation (step 2 or 6 in figure 1). Because ESFRS is a two-step process, now the relaxation (step 5 or 3) is automatically also resonant, thus this process is double resonant, yielding an extremely pronounced efficiency enhancement.
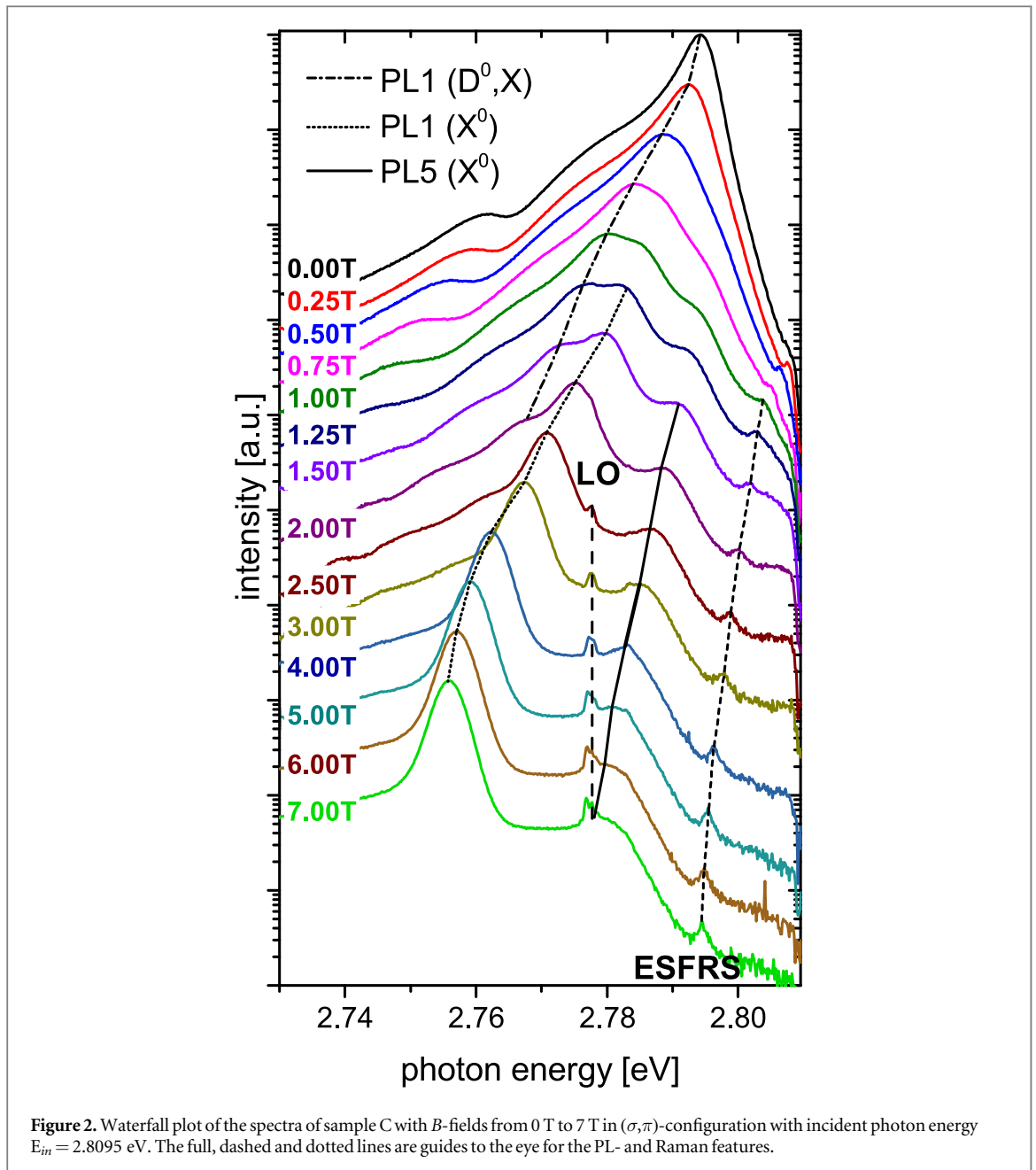
The resonance profile of the ESFRS (i.e. the ESFRS peak intensity versus the incident photon energy) is therefore a powerful and sensitive method to analyze the energy distribution of the dopant electron states, which is the main goal of this study. Furthermore, the resonantly enhanced ESFRS intensity is a prerequisite for its identification in experimental spectra amongst the strong features of near-bandgap PL from free (X^0) and donor-bound excitons (D^0,X).

The *B*-field-dependent development of the Raman and PL features in near-resonantly excited spectra in (σ,π) configuration is shown in figure 2 exemplarily for Sample C. The by-far most intense features are PL peaks, which were identified as such by their spectral position independent of the employed laser frequency. The *B*-field dependence of the peak positions is plotted in figure 3. The peaks show *B*-induced redshifts according to the Brillouin function. Moreover, the initially dominant peak weakens with increasing *B*-field. Simultaneously a second feature appears, which has an about 5 meV higher energy and dominates already at 1.5 T. These observations are typical for the donor-bound exciton (D^0,X), which gets instable with increasing *B*-field, and the free exciton (X^0) as its substitute in the PL spectrum [28]. Hence we assign these peaks accordingly. The involved transition is identified as step 1 of figure 1, because these peaks have the lowest photon energy and the strongest *B*-induced redshift. Therefore, they are denoted as PL1 (D^0,X) and PL1 (X^0).

A third, weaker PL-line can be identified as transition PL 5 (from $|CB, -1/2\rangle$ to $|VB, -1/2\rangle$) due to its higher photon energy, its lower *B*-induced redshift, and its π-polarization, i.e., its absence for σ-polarized detection (not shown here). In principle, this peak experiences the same change from the (D^0,X) to the (X^0), but due to the overall broad PL features, this switch cannot be resolved experimentally.

Moreover, two Raman features are visible, which were identified as such by their constant Stokes shift when changing the laser line. The peak with a *B*-independent Raman shift of about 255 cm^{-1} originates from the longitudinal optical (LO) phonon [29]. The second Raman peak shows a *B*-field dependence according to the Brillouin function, saturating for $B = 7$ T at a Stokes shift of $\Delta E = 15$ meV, corresponding to 121 cm^{-1}. This peak is attributed to the ESFRS, which directly reflects the *B*-induced spin splitting ΔCB of the conduction band. This ESFRS peak, and specifically the resonance profile of its scattering efficiency, will be the subject of the following discussion.

A prerequisite for the accurate determination of the ESFRS peak intensity is to effectuate a PL background intensity as low as possible at the spectral position of this Raman peak, while at the same time matching resonance with appropriate electronic transitions. This condition can be realized by employing for the ESFRS process the transitions $6\Uparrow$ (from $|VB, +1/2\rangle$ to $|CB, +1/2\rangle$; π-polarized) and $3\Downarrow$ (from $|CB, -1/2\rangle$ to $|VB, +1/2\rangle$; σ-polarized) of figure 1, whose spectral positions are blue-shifted by ΔVB with respect to the transitions $2\Uparrow$ and $5\Downarrow$, and therefore up to 25 meV further away from the dominant PL1 peak. Thus, the

Figure 2. Waterfall plot of the spectra of sample C with *B*-fields from 0 T to 7 T in (σ, π)-configuration with incident photon energy $E_{in} = 2.8095$ eV. The full, dashed and dotted lines are guides to the eye for the PL- and Raman features.

corresponding polarization configuration (π, σ) is the preferential one to study the *B*-field dependence of the ESFRS resonance [20]. We will denote this resonance as the $(6 \Uparrow; 3 \Downarrow)$ ESFRS resonance.

Figure 4 shows a series of (π, σ) spectra of sample C at $B = 7$ T, excited in the range of the $(6 \Uparrow; 3 \Downarrow)$ ESFRS resonance with different closely spaced incident photon energies between 2.807 eV and 2.837 eV. The laser photon energy values are indicated by the vertical arrows on the abscissa, labeled with the indices A to H. The corresponding ESFRS-peaks, which are labeled by the same indices, are Stokes shifted by 15 meV (~ 121 cm^{-1}). They appear on top of the PL, which here features a rather weak peak due to transition 3, while the strong PL peak from transition 1 is spectrally well separated by 57 meV, as shown in the inset, which covers a broader spectral range. Moreover, in each spectrum the PL1 peak intensity is utilized as an internal intensity calibration for normalizing the ESFRS peak intensity, as shown by the ordinate scalings of the inset and the main frame. Obviously, the ESFRS peak shows a clear intensity maximum when the scattered photon energy coincides with the maximum of PL3. This pronounced ESFRS intensity enhancement reflects the above-mentioned double resonance in equation (5).

For a quantitative analysis of the resonance behavior of this process, each ESFRS peak was fitted by a Lorentzian function. Subsequently, the obtained peak areas, which reflect the ESFRS efficiency, were plotted versus the incident photon energy E_{in}. This plot yields a resonance profile for each value of the *B*-field, as shown
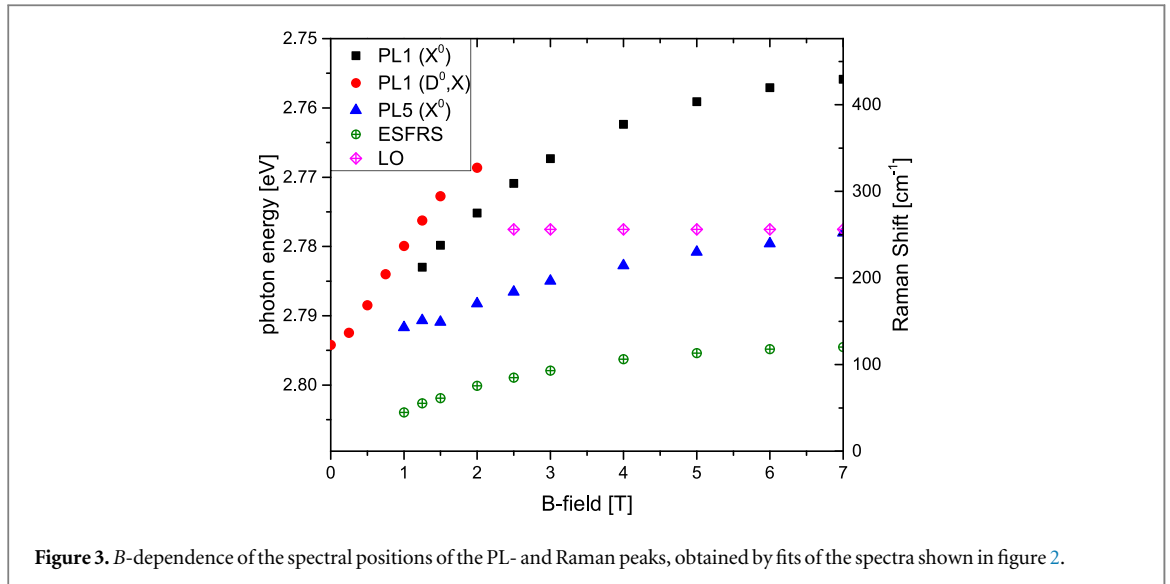
Figure 3. *B*-dependence of the spectral positions of the PL- and Raman peaks, obtained by fits of the spectra shown in figure 2.
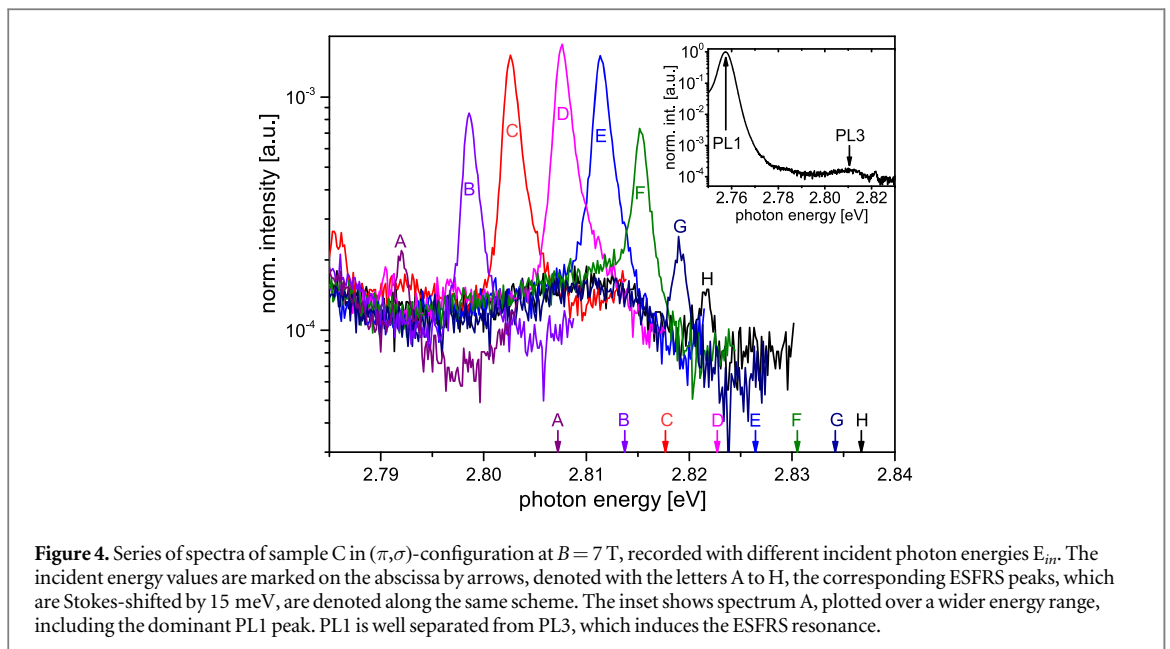

Figure 4. Series of spectra of sample C in (π,σ)-configuration at $B = 7$ T, recorded with different incident photon energies E$_{in}$. The incident energy values are marked on the abscissa by arrows, denoted with the letters A to H, the corresponding ESFRS peaks, which are Stokes-shifted by 15 meV, are denoted along the same scheme. The inset shows spectrum A, plotted over a wider energy range, including the dominant PL1 peak. PL1 is well separated from PL3, which induces the ESFRS resonance.

in figure 5 for various fields between $B = 1$ T to $B = 7$ T. For each *B*-value a partially overlapping double structure appears.

The partially overlapping double structure of each resonance profile was fitted by a pair of Gaussian curves, as exemplarily shown by the dashed and dotted lines for the resonance profile at $B = 7$ T. The spectral separation between the two Gaussians is independent of the *B*-field and amounts to ≈5 meV. This equals the energy difference between the donor-bound exciton (D^0,X) and the free exciton (X^0), as reported in literature [30] and observed in our PL spectra. Therefore, the two resonances are attributed to a (D^0,X)- and an (X^0)-assisted transition. It might be surprising at first glance that the bound exciton (D^0,X) retains its prominent role for the ESFRS efficiency also for $B > 2$ T, because the (D^0,X) becomes instable in higher *B*-fields, as shown in figure 2. However, it has been shown that the (D^0,X) can still dominate the ESFRS process as a transient intermediate state which only needs an extremely short lifetime [20]. For increasing *B*-field, the resonance profile curves show a distinct blue-shift. The (D^0,X) resonance maximum is shifted from 2.806 eV to 2.820 eV. This blue-shift reflects the shift of the dipole transition 6, which is proportional to ΔCB + ΔVB.

The width of the resonance profiles of this sample is in the range of 10 meV, and moreover a clear broadening is observed with increasing *B*-field. In the following, this broadening of the resonance profile will be evaluated in more detail for the purpose of the verification of a *B*-induced widening of the energy distribution of the Cl-donor levels because of their individually different field-induced spin splitting, due to the statistical fluctuations of the local Mn content in their immediate vicinity.
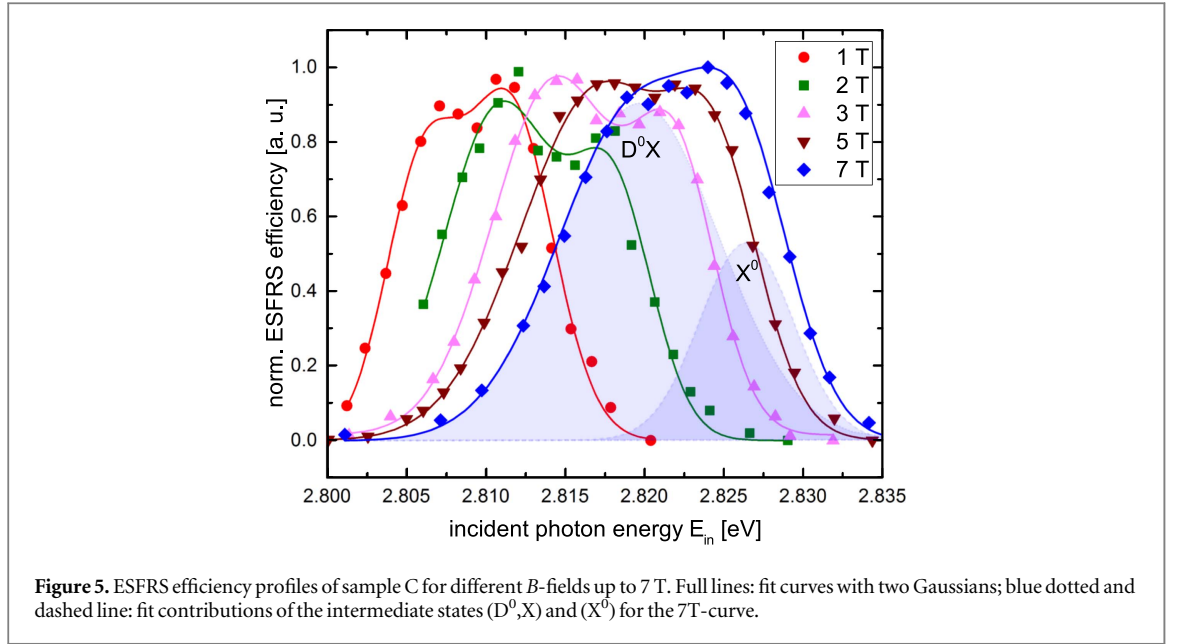
Figure 5. ESFRS efficiency profiles of sample C for different *B*-fields up to 7 T. Full lines: fit curves with two Gaussians; blue dotted and dashed line: fit contributions of the intermediate states (D^0,X) and (X^0) for the 7T-curve.

When assuming a random spatial distribution of the Mn ions on the cation sublattice and the localization of the exciton (D^0,X) on a scale of few nm, each (D^0,X) encompasses in its expansion area a distinct number N_{Mn} of Mn ions, for $Zn_{0.95}Mn_{0.05}Se$, typically $N_{Mn} \sim 50$. This situation is described in terms of a local Mn concentration, denoted as x_{loc}, for each exciton. When considering the x_{loc} values for an ensemble of excitons (D^0,X), a normal distribution is assumed with a FWHM Γ_x around the chemical concentration x_0. As can be seen in equations (1) and (2), the Mn-concentration determines the position of the energy levels in the external *B*-field, thus each exciton (D^0,X) in the ESFRS process has its individual resonance energy. Therefore, the characteristics of the ESFRS resonance curve is affected by the distribution of x_{loc} and thus the chemical half width Γ_x correlates directly with Γ_{res}, the FWHM of the ESFRS resonance.

For a quantitative analysis, we define the concentrations $x^+ = x_0 + \Gamma_x/2$ and $x^- = x_0 - \Gamma_x/2$, and assume a rather narrow distribution, allowing the approximation $T_{AF}(x^+) \approx T_{AF}(x^-)$. Hence using equation (2), we can describe the *B*-field-induced enhancement of Γ_{res} as follows:

$$\Gamma_{res}(B) = \Gamma_0 + \frac{1}{2}[x_{eff}(x^+) - x_{eff}(x^-)] \cdot N_0\alpha \cdot \langle S_z(B) \rangle \tag{6}$$

with Γ_0 as the intrinsic FWHM of the ESFRS scattering process due to the finite lifetime of the intermediate levels in the scattering process, i.e., without taking into account the random distribution of the Mn ions. The incident photon energy E_{in} for which the (D^0,X)-induced maximum of the ESFRS efficiency in figure 5 occurs, systematically depends on the *B*-field and is denoted in the following as $E_{in, res}$. It directly refers to transition 6⇑ in figure 1, and can be expressed as:

$$E_{in,res}(B) = E_0 + \frac{1}{2}(N_0\alpha - \frac{1}{3}N_0\beta) \cdot x_{eff}(x_0) \cdot \langle S_z(B) \rangle \tag{7}$$
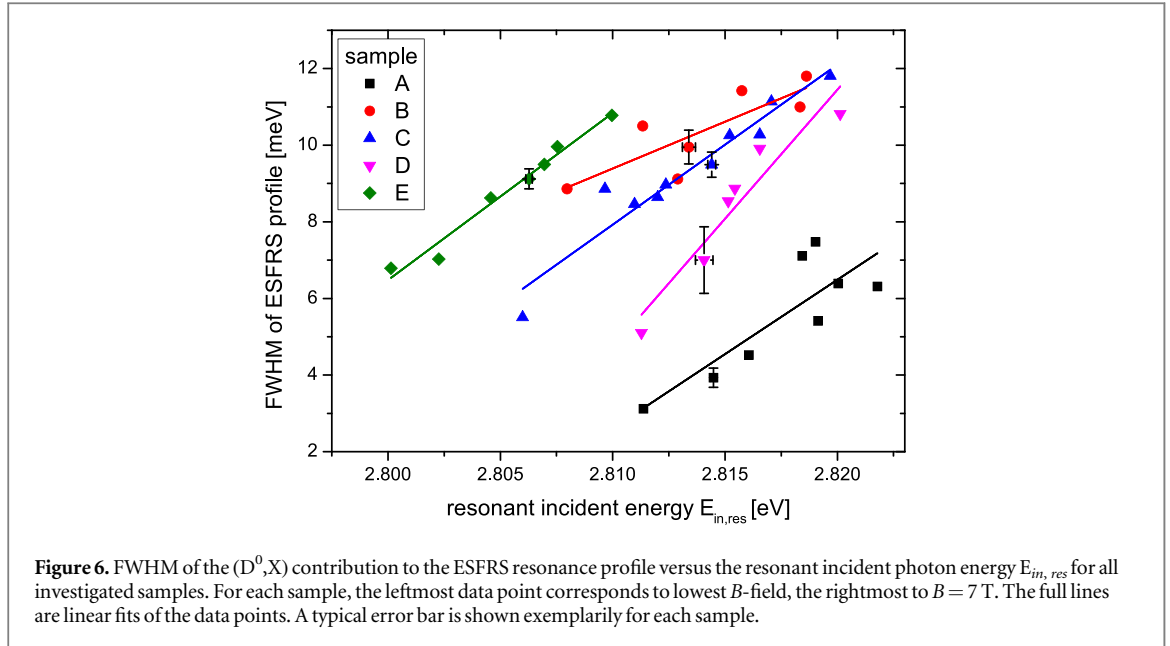
This allows the substitution of equation (7) into equation (6) and gives a linear correlation between the ESFRS resonance width Γ_{res} and the spectral position $E_{in, res}$ of (D^0,X) resonance maximum:

$$\Gamma_{res}(E_{in,res}(B)) = \Gamma_0 + m \cdot [E_{in,res}(B) - E_0] \tag{8}$$

with

$$m = \frac{x_{eff}(x^+) - x_{eff}(x^-)}{x_{eff}(x_0)} \cdot \frac{N_0\alpha}{N_0\alpha - \frac{1}{3}N_0\beta} \tag{9}$$

In figure 6, for each investigated sample the FWHM values Γ_{res} of the Gaussian fits of the (D^0,X)-contribution to the ESFRS resonance profiles are plotted versus the incident photon energy $E_{in, res}$, i.e., the value of E_{in} for which the (D^0,X)-induced ESFRS efficiency maximum occurs. For increasing *B*-values, ranging from 1 T to 7 T, each sample gives rise to a series of data points, the leftmost belonging to the lowest *B*-field and the rightmost to the highest. The FWHM values for the lowest *B*-fields are 3 meV for the intrinsic sample and 5 to 8.9 meV for the doped ones. This difference is attributed to doping-induced lifetime reduction, i.e., enhanced Γ_0. For $B = 7$ T, the values range between 7 meV and 12 meV. The error bars of the Gaussian FWHM values are in the range of 1 meV, induced by the statistical fluctuations of the ESFRS peak intensities. The expected linear increase of the

Figure 6. FWHM of the (D^0,X) contribution to the ESFRS resonance profile versus the resonant incident photon energy $E_{in,res}$ for all investigated samples. For each sample, the leftmost data point corresponds to lowest B-field, the rightmost to $B = 7$ T. The full lines are linear fits of the data points. A typical error bar is shown exemplarily for each sample.

FWHM with increasing $E_{in,res}$ according to equation (8) is observed for all samples, which is a confirmation of the inhomogeneous broadening of the dopant electron level splitting due to the statistical distribution of Mn atoms.

Our Raman results are in full agreement with findings from magneto-transport measurements on the same set of samples. Jansson *et al* observed a giant magnetoresistance in the hopping regime, which is also explained by a similar model [7]. The random distribution of the Mn ions and the localization of donor electrons broadens the energy distribution of the electron levels with increasing B-field, which hinders the electron transport and consequently gives rise to a large positive magnetoresistance. The application of this model to other DMS materials is conceivable and may give further physical insight also for those systems.

Furthermore, for the free-exciton (X^0) resonance in our Raman spectra, no such distinct enhancement of Γ_{res} with increasing B-field is observed. We assign this behavior to the unbound nature of the (X^0), thus it spans over a larger area and captures a higher number of Mn ions. Therefore, the impact of local fluctuations of the Mn concentration on the individual (X^0) should be reduced, which consequently harmonizes the (X^0) energy levels, resulting in a narrower distribution of x_{loc}, i.e., a less pronounced B-induced enhancement of the resonance profile width of the (X^0)-induced ESFRS process.

Beside the characterization of the energy level distribution of the dopant electrons, the quantitative evaluation of the ESFRS resonance curve behavior also enables the approximation of the (D^0,X) radius. This procedure relies on the statistics of the Mn^{2+} incorporation. For a (Zn,Mn)Se crystal with the chemical Mn^{2+} concentration x_0 and a random positioning of the Mn^{2+} ions on the cation sublattice, for each cation site the occupation probability with Mn^{2+} can be assumed as x_0, the Zn^{2+} probability as $(1-x_0)$, yielding a binomial distribution. When considering as intermediate states for the ESFRS process a random set of (D^0,X) excitons, the half-width Γ_x of the corresponding binomial distribution is $\Gamma_x = 2\sqrt{2ln(2)}\sqrt{x_0 \cdot (1-x_0)/N}$, where N denotes the number of cations in the effective volume of the (D^0,X), e.g. for the Mn concentration $x_0 = 0.05$ $\Gamma_{x=0.05} = 0.513/\sqrt{N}$. Equation (9) allows through the first factor on its right-hand side the determination of Γ_x from the slope m of the B-induced ESFRS resonance broadening in figure 6, which for each sample was obtained by a linear fit. Subsequently, the relevant number N of cations in the (D^0,X) volume is determined from Γ_x through the relation for the binomial half-width. Finally, the radius of the (D^0,X) is obtained by considering the presence of four cations per cubic unit cell of the face-centered cubic crystal and the cubic unit cell volume of ZnSe $V = (0.567 \text{ nm})^3$ [31]. The resulting (D^0,X) radii, which were obtained for our samples by this procedure, are between 1.75 nm and 5.90 nm, as listed in table 2. For the three samples B, C, D with $x_0 = 0.05$ and dopant concentrations between $2 \times 10^{17} \text{ cm}^{-3}$ and $1.3 \times 10^{18} \text{ cm}^{-3}$ a decrease of the (D^0,X) radius with increasing dopant concentration is observed, which might be due to an enhanced interaction between the (D^0,X) and therefore leads to a hampering of the expansion of the (D^0,X). Furthermore, with increasing Mn concentration x_0 the radius of the (D^0,X) tends to decrease, as can be seen e.g. by comparing sample E $(x_0 = 0.01)$ and A $(x_0 = 0.07)$. These results are in line with the observation by Kavokin *et al* for a set of $Cd_{1-x}Mn_xTe$ samples, with Mn content varying from 0.1 up to 0.4. Here, based on magneto-optical probing by magnetic polarons, a decrease from 5 nm to 2 nm was reported [32]. Thus, our evaluation of the B-induced broadening of the ESFRS

Table 2. Evaluation of the (D^0,X) radii of the $Zn_{1-x}Mn_xSe:Cl$ samples: Mn contents x_0, doping levels N_{Cl}, slope m of the B-induced ESRFS resonance broadening (from figure 6), FWHM Γ_x of the Mn distribution, and resulting (D^0,X) radii.

sample	Mn x_0	N_{Cl} (cm^{-3})	slope m	FWHM Γ_x	(D^0,X) radius (nm)
A	0.07	$<10^{16}$	0.388	0.023	1.96 ± 0.28
B	0.05	2.0×10^{17}	0.244	0.010	3.53 ± 0.57
C	0.05	4.2×10^{17}	0.418	0.019	2.37 ± 0.14
D	0.05	1.3×10^{18}	0.674	0.028	1.75 ± 0.16
E	0.01	4.3×10^{17}	0.436	0.002	5.90 ± 0.26

efficiency profile on the base of Mn-incorporation statistics constitutes a viable alternative to other established methods for the determination of (D^0,X) radii.

4. Conclusions

In this study, the impact of local fluctuations of the Mn-ion concentration on the dopant electron energy level distribution in an external B-field due to (s-d) exchange interaction was analyzed for a series of (Zn,Mn)Se:Cl samples with Mn contents between 0.01 and 0.07 and a wide range of n-dopant concentrations up to 1.3×10^{18} cm^{-3} by resonant electron spin-flip Raman spectroscopy. The resonance profile of the spin-flip intensity consists of a twin peak structure, which is attributed to the donor-bound-exciton (D^0,X)- and the free-exciton (X^0)-mediated spin-flip process. With increasing external B-field a distinct broadening of the resonance profile was observed, primarily for the (D^0,X) mediated process. This profile broadening is explained as a statistical consequence of the random distribution of the Mn ions on the cation lattice sites together with the localization of the (D^0,X), which causes a widening of the electron energy level distribution with increasing B-field. Due to the non-localized character of the (X^0), no such distinct broadening effect occurs for the latter. From the quantitative analysis of the FWHM of the (D^0,X) resonance profiles for the different Mn contents and dopant concentrations the (D^0,X) radii were evaluated, yieldig values in the range from 1.75 nm to 5.90 nm, decreasing with higher Mn content as well as doping concentration.

Acknowledgments

ORCID iDs

J Geurts https://orcid.org/0000-0001-6838-5312

References

[1] Furdyna J K 1988 Diluted magnetic semiconductors *J. Appl. Phys.* **64** R29–64

[2] Heimbrodt W and Klar P J 2004 *Encyclopedia of Nanoscience and Nanotechnology* 4 (Stevenson Ranch, CA: American Scientific Publishers)

[3] Ramdas A K and Rodriguez S 1988 *Semiconductors and Semimetals* 25 (Waltham: Academic Press, Inc)

[4] Nenashev A V, Jansson F, Wiemer M, Petznick S, Klar P J, Hetterich M, Dvurechenskii A V, Gebhard F and Baranovskii S D 2013 Scaling approach to hopping magnetoresistivity in dilute magnetic semiconductors *Phys. Rev.* B **88** 115210

[5] Michel C, Klar P J, Baranovskii S D and Thomas P 2004 Influence of magnetic-field-induced tuning of disorder and band structure on the magnetoresistance of paramagnetic dilute magnetic semiconductors *Phys. Rev.* B **69** 165211

[6] Jansson F, Baranovskii S D, Gebhard F and Osterbacka R 2008 Effective temperature for hopping transport in a gaussian density of states *Phys. Rev.* B **77** 195211

[7] Jansson F, Wiemer M, Nenashev A V, Petznick S, Klar P J, Hetterich M, Gebhard F and Baranovskii S D 2014 Large positive magnetoresistance effects in the dilute magnetic semiconductor (Zn,Mn)Se in the regime of electron hopping *J. Appl. Phys.* **116** 083710

[8] Bartholomew D U, Furdyna J K and Ramdas A K 1986 Interband Faraday rotation in diluted magnetic semiconductors: $Zn_{1-x}Mn_xTe$ and $Cd_{1-x}Mn_xTe$ *Phys. Rev.* B **34** 6943–50

[9] Kohl M, Freeman M R, Hong J M and Awschalom D D 1991 Faraday spectroscopy in diluted-magnetic-semiconductor superlattices *Phys. Rev.* B **43** 2431–4

[10] Keller D, Yakovlev D R, König B, Ossau W, Gruber T, Waag A, Molenkamp L W and Scherbakov A V 2001 Heating of the magnetic ion system in (Zn, Mn)Se/(Zn, Be)Se semimagnetic quantum wells by means of photoexcitation *Phys. Rev.* B **65** 035313

[11] Koudinov A V, Kusrayev Yu G, Zakharchenya B P, Wolverson D, Davies J J, Wojtowicz T, Karczewski G and Kossut J 2003 Spin-flip Raman scattering in semi-magnetic quantum wells with in-plane anisotropy: Analysis of the intermediate states *Phys. Rev.* B **67** 115304

[12] Petrou A, Peterson D L, Venugopalan S, Galazka R R, Ramdas A K and Rodriguez S 1983 Raman scattering study of the magnetic excitations in diluted magnetic semiconductors in the presence of an external magnetic field *Phys. Rev.* B **27** 3471–82

[13] Stühler J, Hirsch M, Schaack G and Waag A 1994 Raman spectroscopy of the paramagnetic spin flip in $Cd_{1-x}Mn_xTe$, the role of band-gap excitons as intermediate states, and optically detected electron-nuclear double resonance *Phys. Rev.* B **49** 7345–56

[14] Davies J J, Wolverson D, Karimov O Z and Griffin I J 2000 Spin-flip Raman scattering studies of II-VI heterostructures *J. Cryst. Growth* **214** 616–24

[15] Lentze M, Grabs P, Geurts J, Rönnburg K, Mohler E and Roskos H 2007 Carrier-density dependence of the exchnage coupling between magnetic ions and conduction band electrons in heavily n-type $Zn_{1-x}Mn_xSe$ and optically pumped $Cd_{1-x}Mn_xTe$ *Int. J. Mod. Phys.* B **21** 1632–7

[16] Sapega V F, Ruf T and Cardona M 2001 Spin-flip raman study of exchange interactions in bulk GaAs:Mn *physica Status Solidi (B)* **226** 339–56

[17] Merkulov I A, Yakovlev D R, Keller A, Ossau W, Geurts J, Waag A, Landwehr G, Karczewski G, Wojtowicz T and Kossut J 1999 Kinetic exchange between the conduction band electrons and magnetic ions in quantum-confined structures *Phys. Rev. Lett.* **83** 1431–4

[18] Richter W 1976 Resonant Raman scattering in semiconductors *Springer Tracts in Modern Physics* **78** 121

[19] Cardona M 1982 *Light Scattering in Solids II* (Berlin Heidelberg: Copyright Springer-Verlag)

[20] Hirsch M, Meyer R and Waag A 1993 Excitons as intermediate states in spin-flip raman scattering of electrons bound to donors in $Cd_{1-x}Mn_xTe$ epilayers *Phys. Rev.* B **48** 5217–24

[21] Agarwal K C, Daniel B, Klingshirn C and Hetterich M 2006 Phonon and free-charge-carrier properties of $Zn_{1-x}Mn_xSe$ epilayers grown by molecular-beam epitaxy *Phys. Rev.* B **73** 045211

[22] Twardowski A, Dietl T and Demianiuk M 1983 The study of the s-d type exchange interaction in $Zn_{1-x}Mn_xSe$ mixed crystals *Solid State Commun.* **48** 845–8

[23] Hecht E 2016 *Optics* 5th (Cambridge: Pearson)

[24] Gaj J A and Kossut J 2010 *Introduction to the Physics of Diluted Magnetic Semiconductors* vol 1 (Berlin: Springer)

[25] Damen T C, Porto S P S and Tell B 1966 Raman effect in zinc oxide *Phys. Rev.* **142** 570–4

[26] Twardowski A, von Ortenberg M, Demianiuk M and Pauthenet R 1984 Magnetization and exchange constants in $Zn_{1-x}Mn_xSe$ *Solid State Commun.* **51** 849–52

[27] Shapira Y, Foner S, Ridgley D H, Dwight K and Wold A 1984 Technical saturation and magnetization steps in diluted magnetic semiconductors: Predictions and observations *Phys. Rev.* B **30** 4021–3

[28] Heiman D, Becla P, Kershaw R, Ridgley D, Dwight K, Wold A and Galazka R R 1986 Field-induced exchange effects in (Cd,Mn)Te and (Cd,Mn)Se from photoluminescence measurements *Phys. Rev.* B **34** 3961–9

[29] Riccius H D 1968 Infrared lattice vibrations of zinc selenide and zinc telluride *J. Appl. Phys.* **39** 4381–2

[30] DePuydt J M, Smith T L, Potts J E, Cheng H and Mohapatra S K 1988 Detection and control of impurity incorporation in MBE-grown ZnSe *J. Cryst. Growth* **86** 318–23

[31] Madelung O, Rössler U and Schulz M 1999 Zinc selenide (ZnSe) band structure: Datasheet from Landolt-Börnstein—Group III Condensed Matter *II-VI and I-VII Compounds; Semimagnetic Compounds* Vol 41B (Berlin: Springer-Verlag) (https://doi.org/10.1007/10681719_413)

[32] Kavokin K V, Merkulov I A, Yakovlev D R, Ossau W and Landwehr G 1999 Exciton localization in semimagnetic semiconductors probed by magnetic polarons *Phys. Rev.* B **60** 16499–505